Interface effects on heat dynamics in embedded metal nanoparticles during swift heavy ion irradiation

Jantunen, Ville

2022-07-07

Jantunen , V , Leino , A , Veske , M , Kyritsakis , A , Vazquez Muinos , H , Nordlund , K & Djurabekova , F 2022 , ' Interface effects on heat dynamics in embedded metal nanoparticles during swift heavy ion irradiation ' , Journal of Physics. D, Applied Physics , vol. 55 , no. 27 , 275301 . https://doi.org/10.1088/1361-6463/ac5fd1

http://hdl.handle.net/10138/350948
https://doi.org/10.1088/1361-6463/ac5fd1

acceptedVersion

Interface effects on heat dynamics in embedded metal nanoparticles during swift heavy ion irradiation

Ville Jantunen[1], Aleksi Leino[1], Mihkel Veske[2], Andreas Kyritsakis[2], Henrique Vasquez Muinos[1], Kai Nordlund[1], Flyura Djurabekova[1]

[1]University of Helsinki, Department of Physics, P.O. Box 43, FI-00014 Helsinki, Finland

[2] University of Tartu, Faculty of Science, Institute of Technology, Nooruse 1 Tartu, EE 50411

E-mail: ville.jantunen@helsinki.fi

Submitted: November 2021

Abstract. Swift heavy ion-induced shape modification of metal nanoparticles embedded in an insulating matrix has been reported in many experimental studies. The shaping process was studied theoretically by modeling transport of the heat generated by electron excitations during a swift heavy ion impact on the embedded nanoparticle. These models have assumed that the interface between the matrix and the metal does not alter the heat flow. However, the difference between the Fermi level of the metal and the bottom of the conduction band in the insulator may result in a significant energy barrier that obstructs the free flow of the heat carried by energetic electrons. Moreover, the interface may enhance electron-lattice scattering and resist lattice heat conduction.

In this work, we use the finite-element method (FEM) to solve partial differential equations for heat conduction through the interface between the metal nanoparticle and the insulating matrix including interface effects. Based on an exemplary case of a gold nanoparticle embedded in a silica matrix, we study how the processes at the interface may alter the heat transport through it. We observe that obstruction at the interface impacts mainly the timescale and efficiency of material melting. Each of the studied effects changes the size and shape of the nanoparticle regions, where the temperature rises above the melting point.

Understanding the role of the interface on heat dynamics during swift heavy ion impacts can improve estimations of the maximal size of embedded nanoparticles that are still susceptible to shape modification by

energetic ions. The accuracy of model predictions can be crucial for the development of nanoscale optoelectronic applications.

Keywords: Two-temperature model, nanoparticle, interface, swift heavy ions

Submitted to: *J. Phys. D: Appl. Phys.*

1. Introduction

Metal nanoparticles (NPs) have interesting effects on the optical properties of materials depending on their shape and orientation. This dependence offers a spectrum of possible future applications in optical devices [1, 2]. One way to manipulate shapes of nanoparticles, while keeping them aligned, is to embed or to grow them inside of an insulating matrix and subsequently irradiate by swift heavy ions (SHI) [3–17]. SHIs are highly energetic ions that slow down primarily via the electronic stopping, i.e. depositing energy to the electronic subsystem. Generally, electronic stopping power in metals is high [18], hence, a SHI impact on a metal NP results in a large amount of energy deposited to the electrons along the ion trajectory. This leads to the very high energy density deposited along the ion track, which can easily be sufficient to melt or even vaporize the NP. However, the strong heat conduction by free electrons in these materials dissipate the energy away from the track, drastically reducing the heating effect. However, in metal NPs, the energy dissipates among a limited number of metallic atoms. Moreover, the energy deposition to the NP increases linearly with the particle diameter, but melting and vaporization are dependent on the particle volume. The larger the NP, the lesser the effects are observed. For instance, Rizza et al. [19] showed that the ions that were able to induce the shape modification of smaller NPs, did not change the shape of NPs larger than 80 nm. The inelastic thermal spike model (*i*-TS) [20] or, more generally, two-temperature model (TTM) [21, 22], and its implementations within the MD

simulations [23] has been successfully applied to explain the shape modification of metal NPs by swift heavy ions [6, 24]. According to this model, the main relevant parameters, which are able to explain the SHI effects are the (electronic) thermal conduction and the rate of energy transfer from electronic to atomic subsystems. The latter is called due to historic reasons the effective electron-phonon (*e-ph*) coupling, which is fairly low for metals. The low *e-ph* coupling and high electronic heat conductivity lead to efficient dissipation of energy far from the track core before it is transferred to the atomic lattice. It explains why tracks in metals are observed only when electronic stopping powers of irradiating ions are very high ($\gtrapprox$ 50 keV/nm) [25, 26]. By contrast, in dielectric materials, such as SiO_2, the *e-ph* coupling is higher by several orders of magnitude. The ion tracks in these materials are observed much more commonly and at lower stopping powers ($\gtrapprox$ 5 keV/nm) [23, 27, 28].

The *i*-TS model has been used to study the spatiotemporal evolution of temperatures away from SHI trajectories [20] [9,29–32]. With the assumption that ion tracks result from local heating of the lattice above the melting point, the model can be parameterized by fitting to experimental track radii. The model can then be used to study the energy transfer between ions and the material or predict new track radii at different irradiation conditions. Combined with molecular dynamics (MD) simulations, the TTM provided deep insights into the mechanisms of damage formation in materials [4, 6, 17, 23, 27, 28]. Moreover, the model was also used to explain the shape modification of embedded metal NPs by either solving analytically the partial differential equations (PDE) for TTM in 3D [33] or by combining TTM with MD simulations [4, 6, 24]. Analytical solution of the PDEs for shape modification of NPs is an attractive approach, since it can give a reasonable estimation of shape evolution for relatively low computational costs, even if the size of the NP is several tens of nanometers.

According to the model suggested by Dufour *et al.* [33], which was developed for the prediction of shape evolution of Au NPs embedded in *a*-SiO_2, the energy deposited to the electrons in Au

NP's is not transferred to the Au atoms. Instead, the model predicts that hot electrons quickly spread away from the NP. They pass through the interface to the surrounding silica matrix with no obstruction. Here, because of much lower electronic heat conductivity and much higher electron-phonon coupling than in gold, the hot electrons do not diffuse far but deposit their energy in silica in the close vicinity to the NP. This energy was sufficient to melt the surrounding material, consequently melting the NP as well. In these calculations, the heat transfer through the interface is unaffected by its electronic structure. However, since a-SiO_2 is an insulator with a large band gap, there is a significant energy difference between the bottom of the conduction band of silica and the Fermi level in Au. In other calculations [14], by contrast, it has been assumed that this energy difference acted as a barrier for heat conduction at the interface, affecting the heat flow through it or even completely preventing it. To resolve the clear discrepancy between the two approaches and deem which one is more appropriate, calculations that consider explicitly an electron transfer barrier between a metal NP and an insulator matrix are needed.

In this work, we solve numerically the time-dependent PDEs for two-temperature modeling in the 3D geometry for Au NPs embedded in a-SiO_2. Unlike the model in [33], however, we use more flexible mesh of the finite element method (FEM) to increase computational efficiency and allow for compatibility with MD simulations [34]. The FEM formulation also allows us to add conditions that limit the heat flow at the silica/Au interface partially. In the previous approaches, the interface was considered to be either fully transparent [33] or insulating [14] thermally. We include the electron transition barrier in the metal-insulator interface to analyze the dynamics of electrons resulting in energy deposition to both a-SiO_2 and Au atoms. We take into consideration the electron energy distribution to estimate the number of electrons that have sufficient energy to pass to the conduction band of silica. We use this approach to study the thermal evolution within NPs of different sizes to assess the amount of heat developed in NP after a SHI impact that is available for the shape transformation. For clarity and concreteness, we will refer to these cases as

NP(X) with X in the parenthesis indicating the diameter of NP in nm. We also extend our model to the cylindrical nanorods (NR), which will be referred to as NR($X\times Y$), where X is the length and Y is the minor diameter of the NR given also in nm. Finally, we consider the effect of the interface on electron-lattice scattering and lattice heat conduction in large (d$\geq$ 40 nm) spherical nanoparticles.

2. Methods

2.1. Two temperature model

To describe the process of heat exchange between electronic and atomic subsystems, we use the TTM, which is expressed by two heat diffusion equations:

$$c_{v,e}\frac{dT_e}{dt} = \nabla\cdot(\kappa_e\nabla T_e) - g\cdot(T_e - T_a) + S(r_\perp, z) \quad (1)$$

$$c_{v,a}\frac{dT_a}{dt} = \nabla\cdot(\kappa_a\nabla T_a) + g\cdot(T_e - T_a) \quad (2)$$

where c_v is the volumetric heat capacity, κ is the heat conductivity and g is the *e-ph* coupling term, which is responsible for energy exchange between the electronic (subindex e) and the atomic (subindex a) subsystems. For the energy source term S($r_\perp$,z), we use the Waligorski formula [35] normalized to give the electronic stopping power as predicted by SRIM [18] software (for more details, see [23]). $r_\perp$ and z are the distances radially from and linearly along the ion trajectory, respectively. In the current geometry, there are two media, Au and a-SiO_2, which an ion passes on its way through the cell. We compute the S($r_\perp$,z) profile by joining the independently calculated profiles for the bulk Au and the bulk a-SiO_2 cells as follows. The joint profile assumes the value either for Au or for a-SiO_2 depending on which of the two materials is found at the given coordinate ($r_\perp$,z). We chose not to include yet a time dependence of S($r_\perp$,z), since in the current simulations we do not follow the dynamic evolution of the NP shape, but rather analyze the effect of the initial

NP geometry and the effect of an energy barrier for hot electrons in order to assess the amount of energy, which is initially available for the shape modification.

We solve the time-dependent Eqs.(1) and (2) using the FEM-code FEMOCS [34,36] with the modifications explained in Appendix B. For consistency, we used the same TTM parameters and the same ion (Br 110 MeV) as in [33]. The summary of these parameters can be found in Appendix C.

To verify the current model, we performed the calculations with the same assumptions as in the model of [33], i.e. considering no energy barrier in the interface and for the same geometry. The detailed comparison of both results is shown in Appendix A and confirms that despite the different numerical methods used for solving the PDEs of the TTM, the present model and the model in [33] predict the same heat evolution dynamics in the system with an embedded NP.

2.2. Nanoparticle - insulator interface

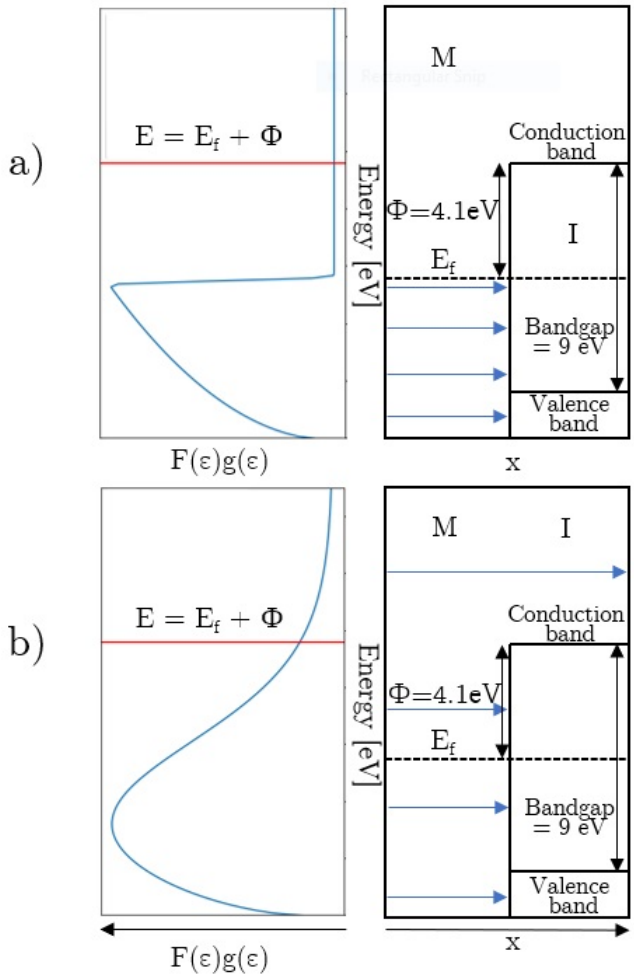

Figure 1: Schematic presentation electronic structre of the metal(M)-insulator(I) interface in the case of a) low (top) and b) high electronic temperatures (bottom). On the left hand side the Fermi-Dirac distribution function multiplied by a density of states are shown. Band bending is omitted in the diagram for simplicity.

A schematic presentation of the electronic structure at the metal NP-dielectric interface is given in Figure 1. In the Figure, we show the Fermi-Dirac distribution function and a simplified electronic

structure of the interface. The electrons need to overcome a barrier given by Φ to reach the conduction band of silica.

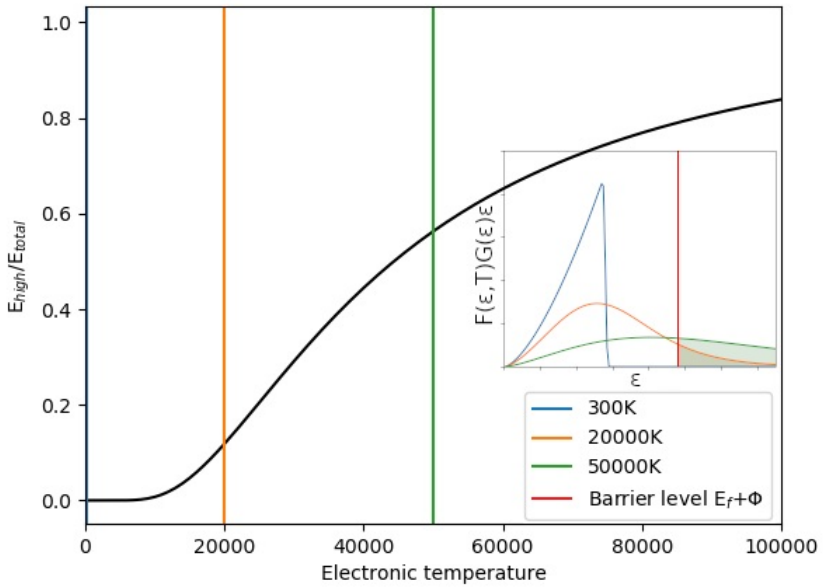

Figure 2: Proportion of electron energy above barrier level $\mathrm{E}_{high}(\mathrm{T})/\mathrm{E}_{total}(\mathrm{T})$ as a function of temperature. Portion of the integrals (coloured) above the barrier line (red) compared to the total integral are the same as the values in $\mathrm{E}_{high}(\mathrm{T})/\mathrm{E}_{total}(\mathrm{T})$ at corresponding temperatures.

We take into account the energy barrier by reducing the heat flux through the interface. This reduction depends on the number of electrons with the energy below the height of the barrier. For this, we calculate the ratio of the total energy of the electrons with the energy above the energy barrier to the total energy deposited to the electronic subsystem: [37, p. 44]

$$\frac{E_{\mathrm{high}}(T_e)}{E_{\mathrm{total}}(T_e)} = \frac{\int_{E_b}^{\infty} G(\varepsilon)F(\varepsilon,T_e)\varepsilon d\varepsilon}{\int_{0}^{\infty} G(\varepsilon)F(\varepsilon,T_e)\varepsilon d\varepsilon} \tag{3}$$

where $G(\varepsilon)$ is the density of states, $F(\varepsilon,T)$ the Fermi-function and ε the electron energy. The evolution of the ratio $\frac{E_{\mathrm{high}}(T_e)}{E_{\mathrm{total}}}$ as a function of electron temperature is shown in Figure 2, while

the inset shows the distribution of electrons multiplied by their energy as a function of energy. We incorporate this factor into Eqs. 1 and 2, within the Neumann boundary condition of 1 at the boundary between the electronic subsystems of gold and a-SiO_2

$$\begin{aligned} q_{Au}(\mathbf{x}) = -k_{\mathrm{Au}} \frac{\partial T_{e,\mathrm{Au}}}{\partial \mathbf{n}}(t,\mathbf{x}) = \frac{1}{\alpha} \frac{E_{\mathrm{high}}(T_{e,\mathrm{Au}})}{E_{\mathrm{total}}(T_{e,\mathrm{Au}})} (T_{\mathrm{e,\ Au}}(\mathbf{x},t) - T_{e,\mathrm{SiO_2}}(\mathbf{x},t)) \\ q_{\mathrm{SiO_2}}(\mathbf{x}) = k_{\mathrm{SiO_2}} \frac{\partial T_{e,\mathrm{SiO_2}}}{\partial \mathbf{n}}(t,\mathbf{x}) = q_{Au}, \qquad \forall \mathbf{x} \in \partial\Omega_{\mathrm{Au/SiO_2}} \end{aligned} \tag{4}$$

where $\mathbf{x}$ is the three-dimensional position vector, $\partial\Omega_{\mathrm{Au/SiO_2}}$ is the boundary between gold and silica, $\mathbf{n}$ is the normal vector of the boundary surface and q is the reduced heat flux density. Subindices are used to separate derivatives and flux at different sides of the boundary. α is a free parameter related to interface thermal resistance (see Section. 4 and Appendix B for more details) chosen such that the model produces unobstructed heat flow through the interface when the barrier is not present, i.e. when $\frac{E_{\mathrm{high}}(T_e)}{E_{\mathrm{total}}(T_e)} = 1$ (see Appendix B). We use the Dirichlet boundary condition at the end of the silica cell, i.e. T = 300 K, in the x and y directions. Periodic boundaries are applied in the z direction.

For the density of states, we use the Drude-Sommerfeld model for the three-dimensional Fermi gas [37, p. 44]:

$$G(\varepsilon) = \frac{3n_e}{2E_f}\sqrt{\frac{\varepsilon}{E_f}}, \qquad \varepsilon > 0 \tag{5}$$

$$G(\varepsilon) = 0, \qquad \varepsilon <= 0 \tag{6}$$

where n is the electron density and E_f (= 5.53 eV) is the Fermi energy. We also assume one free electron per a Au atom. The chemical potential $\mu(T_e)$ in the Fermi function

$$F(\varepsilon, \mu(T_e), T_e) = \frac{1}{e^{(\varepsilon-\mu)/k_b T_e} + 1} \tag{7}$$

is normalized so that the electron density stays constant, i.e. to satisfy the integral

$$n_e = \int_0^\infty G(\varepsilon) F(\varepsilon, \mu(T_e), T_e) d\varepsilon. \tag{8}$$

While an estimate of Φ value can be obtained using the work function of gold and electron affinity of silica, it cannot be accurately deduced from the simple theoretical considerations. We use an experimental value of Φ=4.1 eV from [38]. The value depends on the alignment of the band structures at the contact, which can be understood using the interface dipole theory [39]: No charge transfer is possible between Au and silica because of the energy difference between the Fermi-level in Au and the bottom of the conduction band in silica. However, the electrons can accumulate at the interface occupying the interface states and giving rise to an electric field. This electric field causes alignment of charge neutrality level in silica and the Fermi level in gold.

We note that the effects from electric fields (band bending) are not explicitly included in the current model. As a first approximation, we consider only the barrier when electrons move from silica to gold, quantified by Φ. Moreover, the local electron temperature fully determines the states electrons occupy, and the conservation of electrons in the chemical potential implies charge neutrality. Hence, if charge transport occurs across the barrier from gold to silica, it is implied that a balancing flow follows from silica to gold. The model predicts that the temperature drops very rapidly near the interface in silica. Therefore, the hot electrons do not diffuse far from the interface; no more than a nanometer in order of magnitude. The model assumes that despite the elevated electron temperature, the thermodynamic properties of silica in this region or in the ion track in silica do not change significantly. More elaborate models could be, in principle, used to study the validity of these assumptions.

3. Results

We performed the calculations for Au NP of three different geometries embedded in a-SiO_2 matrix: small spherical NP(20), large spherical NP(40) and the nanorod NR(80×40).

3.1. Temperature evolution within nanoparticles

Figure 3 shows that the thermal dynamics in the system with a NP(20) is very rapid. The energy deposited by the ion to the electrons both in Au and in a-SiO_2 rapidly melts the NP. For this size of NPs, the effect of the barrier at the Au NP-a-SiO_2 interface is not significant. In both simulations, with no barrier (Figure 3a) and with the interface barrier of 4.1 eV (Figure 3b), the electronic temperature at the interface is very high and allows for the heat flow through the interface almost identically in both simulations. Hence, we conclude that the effect of the interface for NPs ($\leq$ 20 nm, at least) is negligible and can be largely ignored within the two-temperature model of SHI effects in NPs. In both our simulations, the NPs remained above the melting temperature for tens of picoseconds, as can be seen in Figure 3c, which shows the situation in both cases after 10 ps of the simulation time.

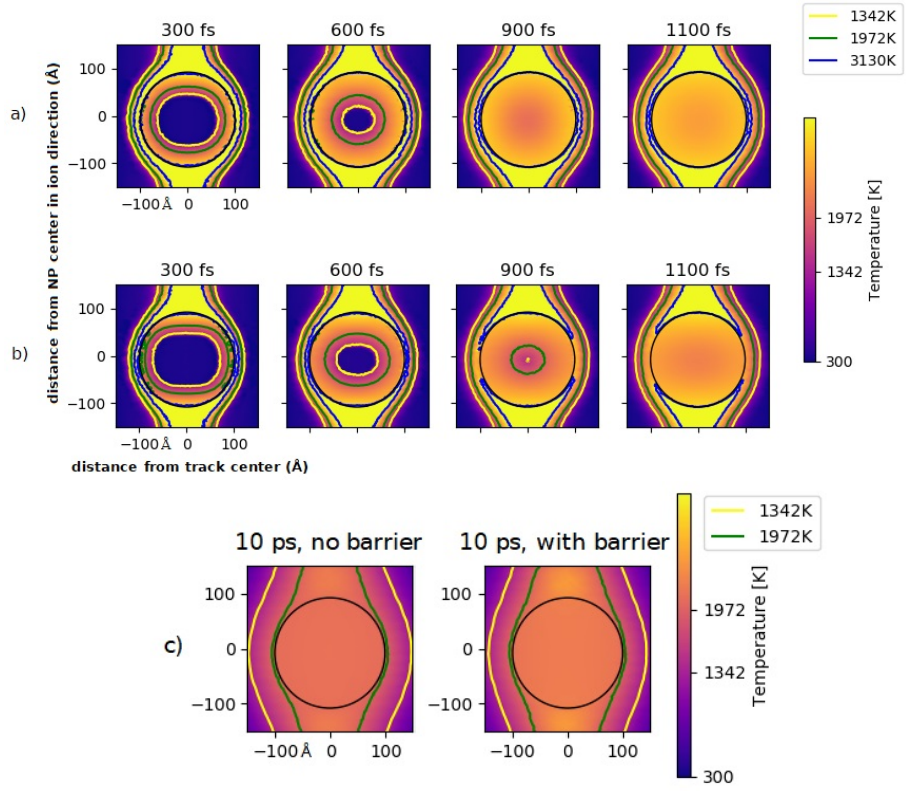

Figure 3: Temperature evolution in NP(20) with a) free thermal transport through the interface and b) barrier $\Phi = 4.1$eV at the interface. c) shows the temperature distribution after 10 ps in the same NP as in a), marked as "no barrier" and in the same NP as in b), marked as "with barrier".

The situation changes in the system with the large NP, see Figure 4. Now we see that the electronic temperature is significantly lower at the NP-a-SiO_2 interface, particularly in the parts along the lateral diameter, which are the furthest from the ion trajectory. Here, the electronic temperature does not reach high values (>20000 K) for an extended time. In these simulations, we observe a clear difference between the simulation runs with the free heat flow through the interface (transparent interface) and with the different barrier values. The result of the former simulation is shown in Figure 4a, while the results of the latter ones are presented in Figure 4b, 4c and 4d, where the color bar indicates the scale of lattice temperature in the system. As we see, the lattice

temperature at the interface along the lateral diameter indeed never reaches the melting point and there is less overall melting within the NP. Due to uncertainty of the barrier height, we also tested three different values of Φ = 3.1 eV, 4.1 eV and 5.1 eV, i.e. by 1 eV below and above the value reported in [38]. For completeness of our study, we have also performed the simulation of heat evolution in the system with NP(20), while the barrier was increased to 5.1 eV. In this simulation, we have not noticed any difference compared to the case with the original barrier of 4.1 eV, which confirms our conclusion of the insignificant effect of the processes at the interface for small size of NPs with d $\leq$ 20 nm.

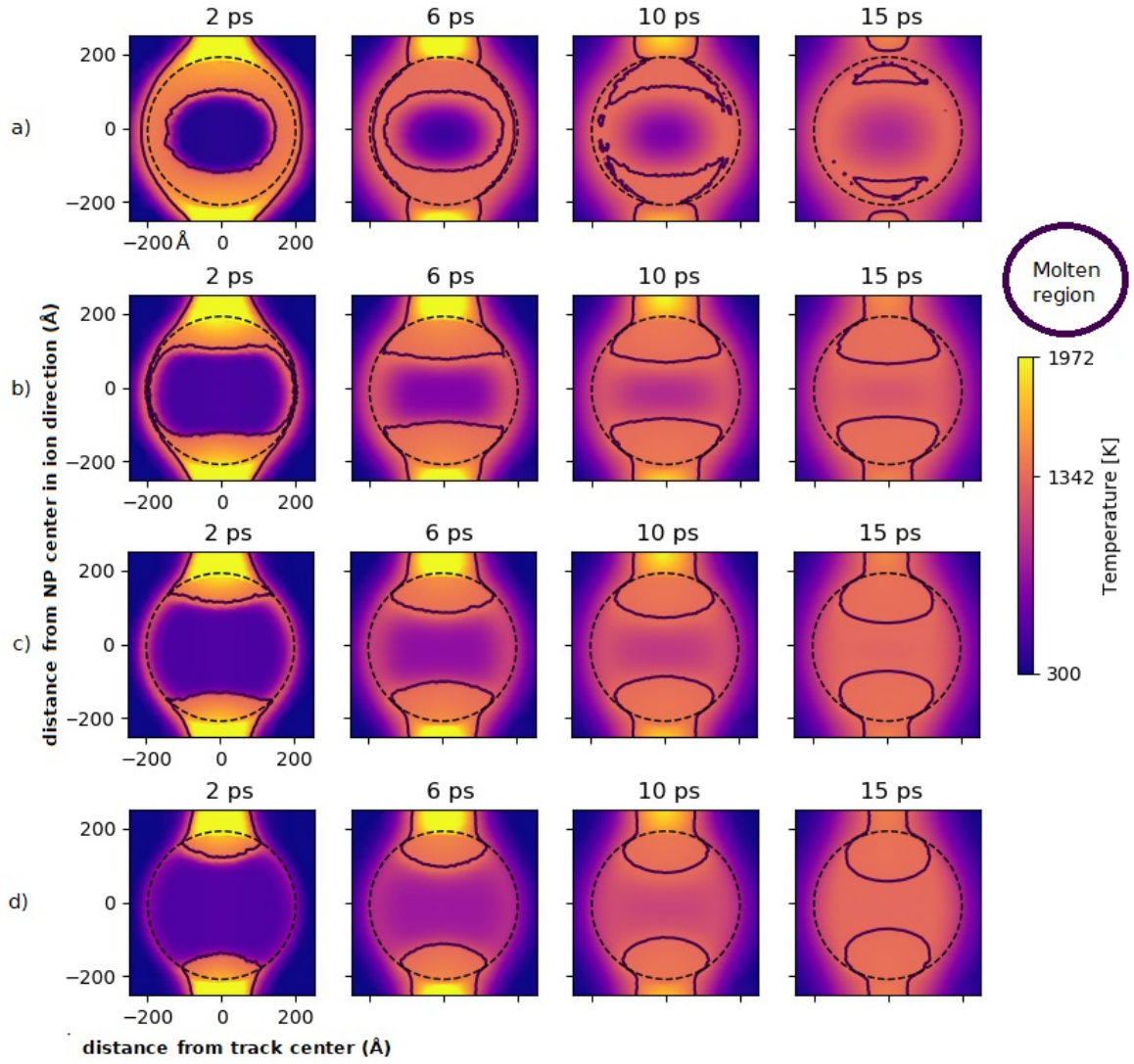

Figure 4: Temperature evolution in the system with NP(40) with a) thermally transparent interface, b) $\Phi = 3.1$ eV (the lowered by 1 eV barrier), c) $\Phi = 4.1$ eV [38], and d) $\Phi = 5.1$ eV (elevated by 1 eV barrier) between the electronic systems of Au and silica. The NP is outlined by the dashed black line. The solid contour lines indicate the regions with atomic temperature above Au melting point.

We further consider the reasons that led to such different heat evolution in the systems with NP(20) and NP(40), when we take into account the energy barrier in the interface. On the other hand, it is also important to understand why the system with NP(20) behaves similarly with and without such an energy barrier. In simulations with NP(20) that has the thermally transparent interface, the NP melts by an indirect heating mechanism as suggested by Dufour et al. [33]. For NP(20) when the barrier is included, the energy of the electrons, when they reach the interface between the small NP and *a*-SiO_2 is so high that the barrier of ∼4 eV does not obstruct the energy transfer through the interface. When the hot electrons reach *a*-SiO_2, they deposit energy to the lattice almost immediately due to high *e-ph* coupling. The hot silica structure in the vicinity of the interface efficiently heats the NP and eventually melts it. In effect, even if electronic heat escapes the NP in form of hot electrons, it returns back to the NP lattice heat.

The dynamics change dramatically when the size of the NP is considerably larger, d≥40 nm. When the NP has the thermally transparent interface, the electronic heat conduction brings the heat to the interface until the electronic system within the NP cools down completely. The initial energy density deposited to the electrons, and, hence, the initial electronic temperatures, within the Au NP decays with the radius as $1/r_{\perp}^2$. This means that at the beginning of the simulation practically the entire interface is cold and the energy exchange takes place only at the top and the bottom of the NP. Because of the high electronic heat conduction in Au, the electronic temperatures in the NP equilibrate very quickly, but not until the electronic temperatures within the NP have already significantly cooled down. This leads to lesser energy deposition at the borders of the NP overall. However, during the first two picoseconds, there is enough heat in the interface that even the sides of the NP along the lateral diameter (the furthest from the track) have melted significantly. This is not the case in the NP with a non-transparent interface. If we include the barrier, there is barely any energy flow through the interface at these furthest borders (sides) as seen in Figure 5, where we show the temporal evolution of energy equilibration (E_{high}/E_{total}, where

indices "high" and "total" indicate the portion of the energy of the electrons above the barrier energy and the total energy of the electrons). As can be seen from Figure 2, after the system has reached 10^3 K there is practically no energy escaping the electronic system of the NP. As a result, the borders of the NP remain through the entire simulations at temperatures below the melting point.

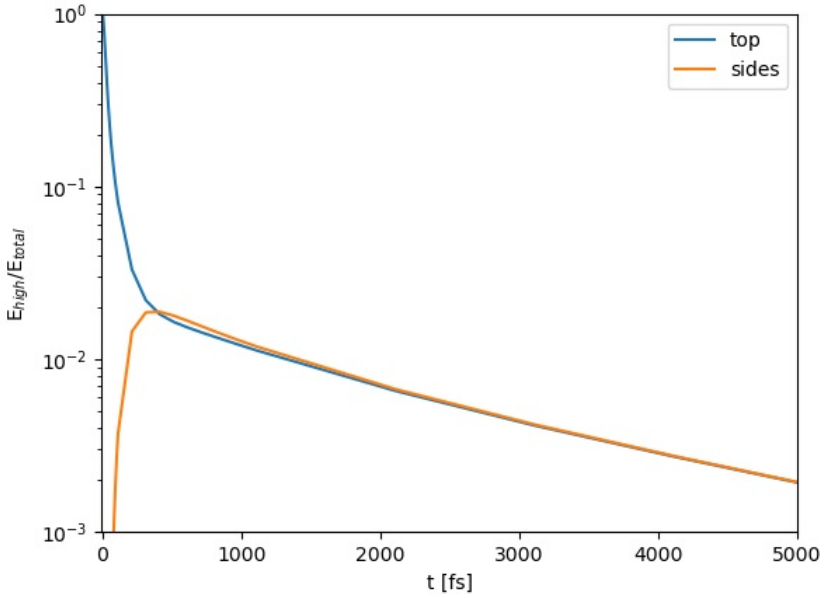

Figure 5: E_{high}/E_{total} as a function of time at the top and sides of the NP in the system with NP(40).

We also observe that the system cools down slower in the simulations with the thermal barrier compared to the simulations with the transparent interface heat flow. In the former case, after reaching the electronic temperature of 10^4 K, the interface becomes practically non-conducting as can be seen in Figure 2. This energy can now only be deposited via *e-ph* coupling within the Au NP, which is a much slower process as the *e-ph* coupling of Au is three orders of magnitude less

than that of silica. The slow heat deposition to the atomic system keeps the NP around 10^3 K for a long time.

We further analyze whether the heat developed in the ion track within silica due to direct energy deposition to this material plays a substantial role in the increased heating of the NP at the top and the bottom where the ion track enters and leaves the NP. We simulated a NP(40) in a hypothetical system with the very high electronic barrier so that the energy is deposited only within the Au NP, but not in silica ($S_{e,\mathrm{SiO_2}} = 0$ eV/nm). These results are shown in Figure 6 and demonstrate that the energy deposition in Au only is sufficient to melt the regions at the top and the bottom of the NP, without contribution of energy deposited in silica. We conclude that the energy initially deposited in Au is the main driving factor of the surface melting, and the asymmetry is not because of the initial energy deposition to silica.

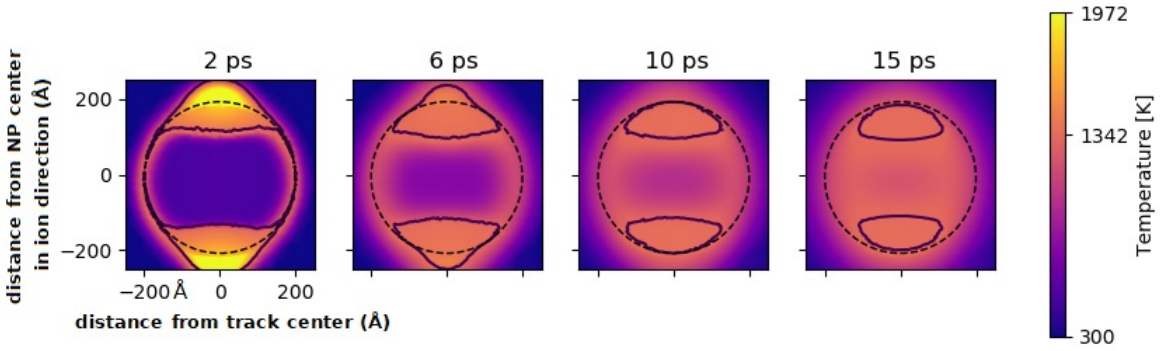

Figure 6: Energy deposition only to the nanoparticle. Contour lines show the regions with the atomic temperatures above the melting point of the NP, while the NP is outlined by the dashed black lines.

Based on these results we conclude that the mismatch between the Fermi level in Au and the bottom of the conduction band in a-SiO_2 at the interface may play a significant role in how the heat flows through the interface, especially when the size of the NPs is not small ($\geq$ 40 nm). The

parts of the interface that the ion intersects along its trajectory (at the top and bottom of the NP) are the closest to the track where the hot electrons are excited. These initially hot electrons pass through these parts of the interface, while by the time Instead, the model predicted that hot electrons quickly spread away from the NP but don't diffuse far within silica because the electronic thermal conductivity and the e-p coupling of gold are notably higher than that of silica. Moreover, the interface does not limit the flow in the model. Consequently, most of the energy was deposited in the silica atoms near the NP. These hot electrons reach the interface along the lateral diameter of the NP they become much cooler and only a very few electrons are able to penetrate through the interface with the barrier. While this is true for both the thermally transparent interface and for the interface with a barrier, the heating dynamics of the NP are different in both cases. When the interface is thermally transparent, all electrons are able to go through it, and even if the electrons are relatively cold, they are still able to deposit sufficient energy to the lattice atoms to heat the NP at the interface melting in the metal structure near the interface. The picture is changing when the barrier is taken into account. Now, the slow electrons can not overcome the barrier, and those which do, transfer much less energy to the surrounding matrix atoms of a-SiO_2 to heat NP significantly. Hence, the NP with the non-transparent interface will not heat up anywhere else except at the top and the bottom of the NP, which are along the ion track.

To summarize the main difference in the behavior of the systems with small (NP(20)) and large (NP(40)) NPs, we draw a schematic that illustrates the processes developing in the interface between an embedded NP and surrounding insulating matrix. In NPs with d $\lesssim$ 20 nm, the dynamics of heat flow through the interface is not affected by the difference in the Fermi level in the metal and the bottom of the conduction band of the insulating matrix, since the temperature of electrons reaching the interface is very high (see the top panel of Figure 7). In a metal NP with d $\sim$ 40 nm, the processes at the interface start playing a significant role. Some of the electrons which reach the interface have cooled down to the values below the energy barrier at the interface.

These electrons are reflected back, where they eventually deposit energy to the lattice in the much slower process of *e-ph* coupling within Au metal. Without taking into account enhanced *e-ph* coupling near the interface due to the increase of the scattering centers for electrons, the melting of the metal surface along the lateral diameter of the particle is not expected (see bottom panel of Figure 7).

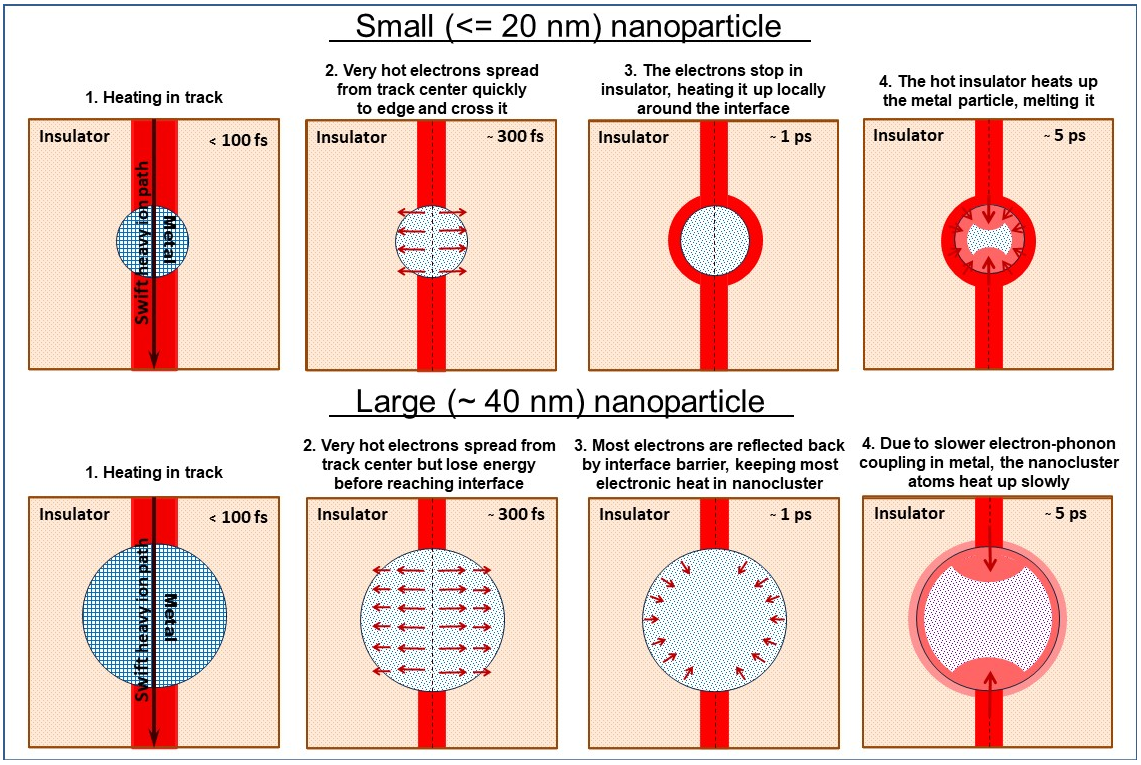

Figure 7: Schematic illustration of heat evolution in NPs after a SHI impact. Note the different behavior of heat evolution for small NPs (d $\leq$ 20 nm) and sufficiently large (d $\approx$ 40 nm), when the electronic barrier in the interface starts playing substantial role in this process.

3.2. Temperature evolution within nanorods

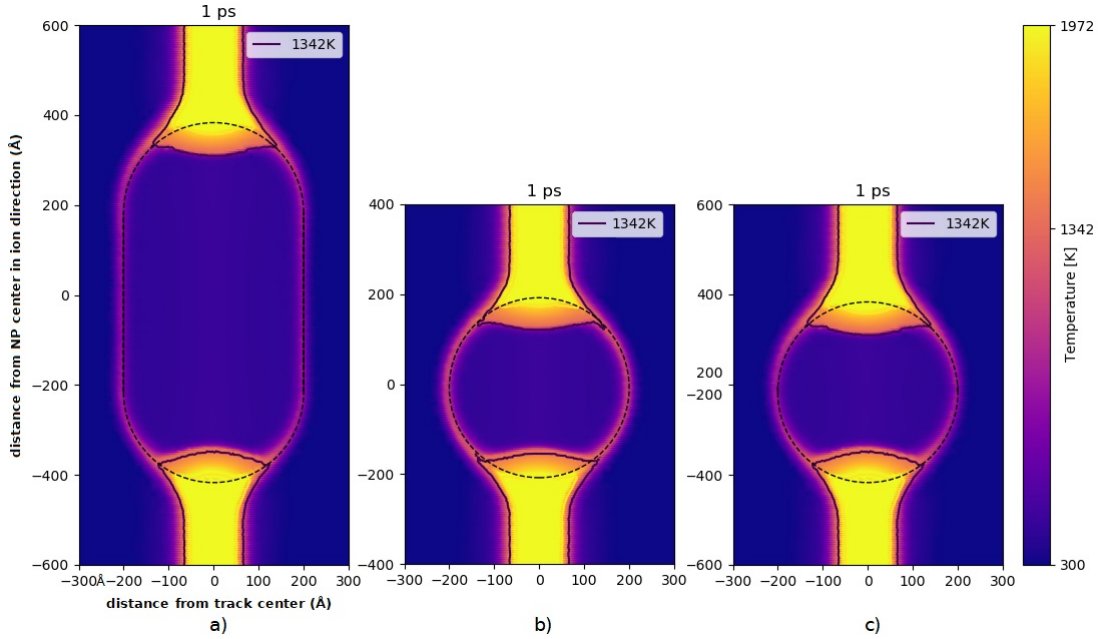

Figure 8: Comparison of temperature distribution in the systems with NR(80×40) (a) and NP(40) (b) after 1 ps from the ion impact. The images show the cross sectional plane through the center of NR and NP parallel to the ion beam. c) shows the same as (a), but the cylindrical part in the middle of the NR is hidden for visualization purpose.

With a few exceptions [10, 40], the studies of the heat flow after SHI impacts have focused on nanospheres. To extend our results to non-spherical NPs, we next study the heat dynamics evolution in cylindrical NRs. NRs could be embedded in silica by depositing a thin film on top of them (see Ref. [10]) and subsequently irradiated to tune their shape. Moreover, at high fluences, spherical NPs were repeatedly reported to elongate into rod-like shapes [19], in which the heat dynamics may differ from that in the initial state of spherical geometry.

The way how the energy is deposited to a NR during a SHI impact may differ from what we

see in a NP because of the elongated shape of the former, since the energy deposition may depend on how the NR is oriented with respect to the ion beam direction. Hence, we now analyze the heat distribution in an elongated NP, i.e. a cylindrical NR. In our simulations we used two sizes of the NRs, NR(80×40) and NR(40×20) with the minor diameters of the same size as the large and small NPs (NP(40) and NP(20)), respectively. It was interesting to note that ion impacts along the major axis of the NRs, the heat flow is very similar to that in the spherical NPs of the same diameter as the minor one of the NR. We observed melting at the top and the bottom tips of the NR, while laterally, the surface of the NR in the middle part of it remained relatively cold. To demonstrate this similarity, we show only the top and bottom parts of the NR in Figure 8c, while hiding the middle (cylindrical) part of it. The temperature profile in Figure 8c is very similar to the one shown in Figure 8b, where the temperature profile developed within the NP of the diameter the same as the minor diameter of the NR is shown.

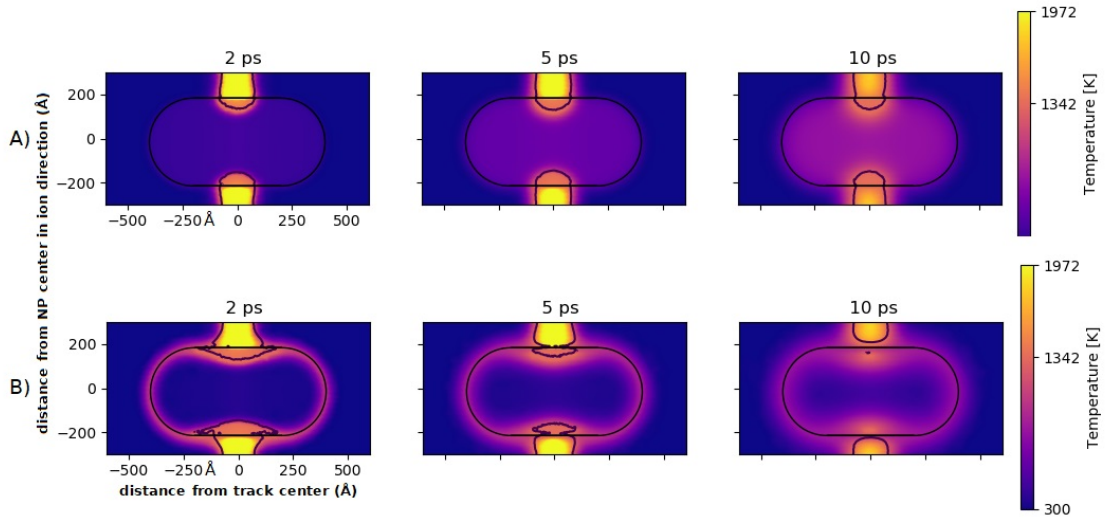

Figure 9: Temperature evolution of NR(80×40) for A) 4.1 eV barrier and B) no barrier.

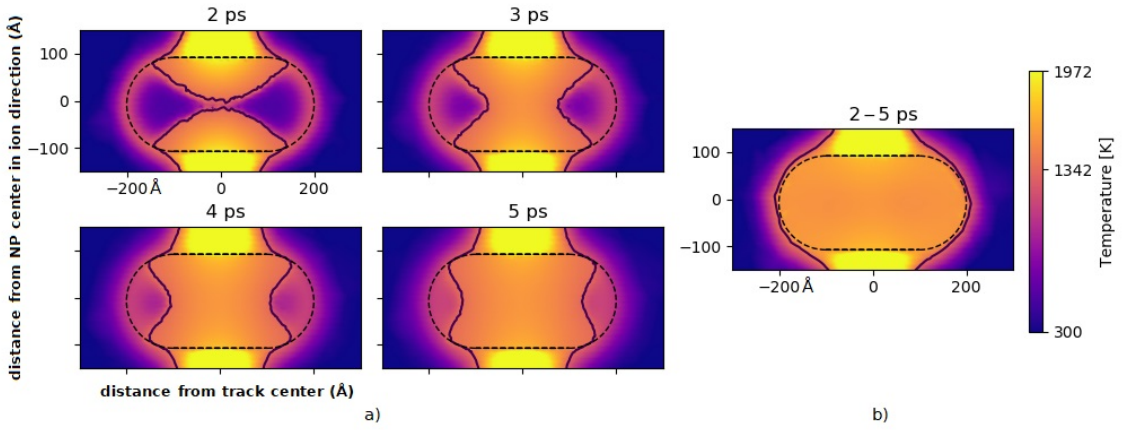

Figure 10: Temperature evolution within the NR(40×20) under different Au/a-SiO_2 interface condition: a) 4.1 eV barrier and b) no barrier.

To see how the temperature evolves if the NR is hit by a SHI through its side, we also performed the simulations with the NRs that are rotated by 90 degrees with respect to the ion trajectory. Initial energy deposition, in this case, is almost identical to the spherical NPs, because the ion now travels the same length (20 nm and 40 nm) in Au as within the corresponding spherical NPs. However, laterally the interface is much further in these simulations than in those with the spherical NPs. In the case of d = 40 nm, the temperature reached the melting value only in the part where the ion hits the NR. This result is shown with the thermally transparent interface in Figure 9a and when a barrier in the interface is taken into account in Figure 9b. The increased distance to the interface reduces the amount of energy, which electrons are able to bring to the lateral interface. This is why even when the interface is thermally transparent, the electrons are not able to carry enough energy to significantly heat the a-SiO_2 structure near the interface. Hence the metal structure near the interface heats up but does not melt. When the barrier is taken into account, the electrons that reached the lateral interface are too cold to overcome the barrier, and heating of the NR proceeds via slow *e-ph* coupling within the NR itself. However, this process

is not sufficiently fast and by the time the energy is transferred to the NR, the temperature is already below the melting point.

When the NR is smaller (NR(40×20)) the difference between the interface with and without a barrier is more pronounced. In the case of no barrier in Figure 10 b) the temperature reaches the melting point within the entire NP. However, when the barrier is added in Figure 10a the temperatures at the lateral interfaces are not high enough to allow for sufficient heat flow through the interface. The melting starts at the top and the bottom of the NR where the ion trajectory crosses the NR/a-SiO_2 interface and expands outwards. However, the temperature near the tips of the NR remains cold (below the melting point). Decreasing the size of the NR even further led to melting of the whole NR even with the barrier as high as 4.1 eV. NRs with a slightly larger radius than 20 nm did not melt fully either with or without the barrier.

4. Heat flow dynamics in the interface

In addition to the existence of the energy barrier for heat flow through the interface, we also pay attention to possible structural effects on the heat dynamics near the interface. The two major contributions which can affect the temperature evolution in this region are enhanced electron scattering at the interface [41] and thermal interface resistance of the lattice [42]. Although both of these phenomena are difficult to measure experimentally, particularly in the geometry of embedded nanoparticles, we offer an analysis of the contribution of these effects within the model proposed above.

We introduce the effect of enhanced scattering in the interface by increasing the effective *e-ph* coupling of Au. The same approach was used in the study of thermal conduction through the flat interfaces in thin films consisting of alternating Au and a-SiO_2 layers [41]. The authors of [41]

took into account the increase of *e-ph* coupling by adding an additional term

$$\pm\frac{h_{es}}{d}(T_e - T_0) \tag{9}$$

to the two-temperature equations Eqs. 1 and 2. In term 9, h_{es} is measured in $Wm^{-2}K^{-1}$ and d is the film thickness. In this film, h_{es} was estimated, and the formulation makes h_{es} independent of the thickness. We implemented this term by increasing the *e-ph* coupling in a thin sphere shell at the surface of the NP, that is, in the outermost shell. The interface heating could be alternatively implemented as a boundary condition as well. In our simulations, we use the same value of h_{es} as in Ref. [41] and $d = 1$ nm, which is the thickness of the shell where the *e-ph* coupling is enhanced. Increasing this parameter twice does not alter significantly the simulation results. While the value of parameter d changes the short timescale dynamics (up to ~ 1 ps), we did not observe relevant differences in long-timescale results and sizes of the molten regions. Here, T_0 is taken to be the lattice temperature of gold as a first approximation. Figure 11 illustrates the heat evolution dynamics, when the enhanced *e-ph* coupling in Au (term given by 9) is taken into account in the vicinity of the interface. We see that now the NP is melting even more efficiently near the surface than in the case when the thermally transparent interface is assumed (Cf. Figure 3a) despite the barrier of 4.1 eV, which is included in these calculations.

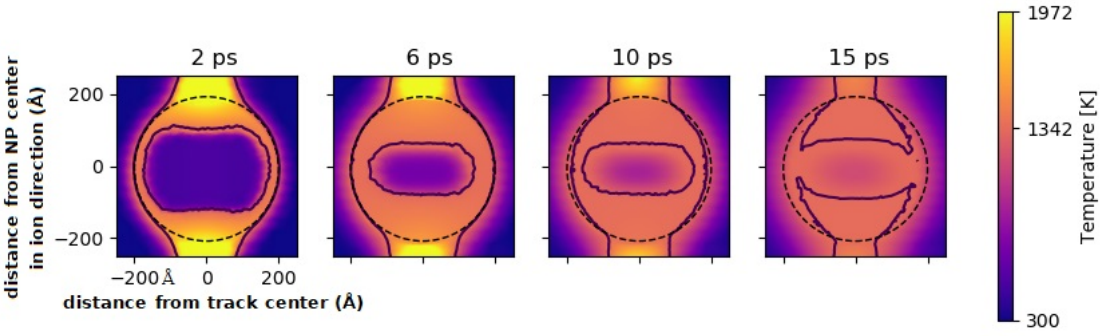

Figure 11: Temperature evolution within NP(40) with the 4.1 eV energy barrier over the interface, taking into account increase of scattering centers for electrons due to defects at the interface.

In addition, the thermal insulation of the interface may also play a role in heat flow through the interface (the relation of thermal insulance to thermal resistance is explained in Appendix B). Previously, this quantity has been estimated for the Au-a-SiO_2 interface (M_I) in layered thin films [42]. We can use it to assess the effect of the insulance on heat dynamics within the embedded NP. In 4 and Appendix B), parameter α has two contributions

$$\alpha = M_{\mathrm{Au}} + M_{\mathrm{SiO_2}} \tag{10}$$

which are needed to describe discontinuity in heat conductivity at the interface. That is, α consists of insulances of Au (M_{Au}) and a-SiO_2 ($M_{\mathrm{SiO_2}}$), which are connected in series analogous to an electrical circuit. This allows us to introduce additional insulance in phonon transport, by adding M_I to the parameter α:

$$\alpha = M_{\mathrm{Au}} + M_{\mathrm{SiO_2}} + M_I \tag{11}$$

Here $M_I = 2.13 \cdot 10^{-8} m^2 K/W$, which is determined as an average of the values reported in [42]. Since it is difficult to isolate the additional insulance of the interface experimentally, this value should be treated as a rough estimation only. The value could also be simulated with atomistic models, provided there is a potential that can describe the Au/a-SiO_2 interactions correctly.

As can be seen in Figure 12a, the increased insulance at the interface increases the fraction of the molten region in the NP. The heat generated in the NP due to increased *e-ph* coupling at the interface is not removed quickly and accumulates within the NP. Subsequently, the NP melts almost entirely. Since there is only a linear increase in total energy deposition with increasing NP radius, NPs with large radii cannot melt even in perfect insulation. To verify that this mechanism does not produce too strong heat in even larger NP, we have performed the simulation also for NP(60). The result shown in see Figure 12b validates that our model does not produce unphysically strong heating to enable melting of significant regions in large NPs, which is in line with the experimental

observations [19]. As we see in Figure 12b, the NP does not melt even with insulation. In this simulation, only the very thin layer near the surface of the NP was molten.

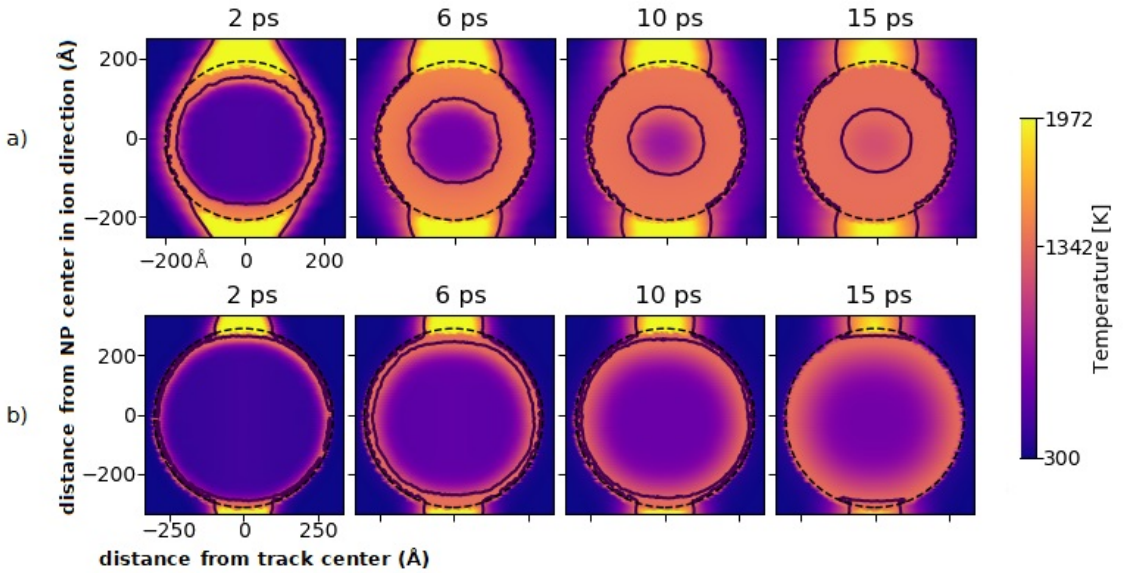

Figure 12: Temperature evolution within a) 40 nm b) 60 nm diameter NPs under 4.1 eV barrier surface scattering with insulance included for the lattice heat conduction.

5. Comparison of interfacial effects on heat dynamics

In this study, we aimed to understand the heat dynamics near the interface and how important the accurate description of processes in this region is for the understanding of shape modification of embedded NPs under SHI irradiation. Conventionally, this issue has been neglected based on an intuitive expectation of a very minor, if any, effect.

Our studies showed that the effect of the barrier in the interface becomes significant if NPs are within a certain size range. This is due to the correlation between the size of the NP and the lateral range of energy decay for the electrons excited by a SHI impact. If a NP is sufficiently large, the energy of the electrons that are reaching the interface region becomes comparable with

the height of the barrier. If so, a large fraction of excited electrons is not able to pass through the interface and remains in the NP, where the energy from electrons is transferred directly to the Au atoms via the slow *e-ph* coupling process. The energy of electrons that were able to penetrate through the barrier is much lower so that even efficient energy deposition in a-SiO_2 will not be able to develop sufficient temperatures to heat the NP.

In the systems with NP(20), the energy of electrons does not yet decay notably by the time, when the electrons reach the interface and they remain very hot while crossing the interface. Hence, the majority of them will freely penetrate through the interface, depositing energy in the a-SiO_2 structure. This result confirms the general assumption of nearly no effect of the barrier on heat flow through the interface, at least, in the NP with a diameter below 20 nm.

We see that the most interesting dynamics of the heat flow for a Br 110 MeV ion develop when the lateral diameter of a NP is above 20 nm. We note that in such cases, the melting of a NP becomes anisotropic, i.e. top and bottom melt much more than the sides, when an energy barrier at the interface is taken into account. The electronic temperature near the interface along the lateral diameter, the furthest from the ion track, does never reach sufficiently high values for effective heat conduction over the interface. Therefore, the surface of these NPs which was not affected directly by the ion track is not expected to melt when the barrier is taken into account, which is contrary to what was found in [33], where no barrier for hot electrons was taken into account. We observe the same behavior even in the NRs with 20 nm in the minor dimension, but positioned perpendicularly to the ion beam. The temperature in these NRs did not reach melting point everywhere. The polar regions of the interface directly affected by the ion track are much closer to the source of hot electrons and the presence of barrier in these regions does not affect the thermal conduction through the interface. More energy is deposited in a-SiO_2 near the interface, inducing the melting of metal structure in these regions. This effect is seen in spherical NPs with d $\geq$ 40 nm, and nanorods with minor d $\geq$ 40 nm.

When we took into account other interface-related effects, the heat flow dynamics over the interface has changed again. For instance, the electron scattering on the surface defects, which enhances the *e-ph* coupling near the interface led to melting of NP surface even when the diameter of the NP was 40 nm. Furthermore, the insulance of the interface adds an additional barrier to the heat flow within the NP. The heat confined in the NP was distributed more evenly, producing symmetrical surface melting with most of the NP melting. The insulance also significantly slowed down the cooling of the NP.

In Figure 13 we summarize the results of all calculations. Temperature evolution in some key regions of the NPs as a function of time can be found in Appendix D. The first row of images, see Figure 13a, show the results of heat dynamics with the transparent interface. In this case, the heat is deposited in the thin a-SiO_2 shell near the NP, which becomes sufficiently hot to melt a significant part of it. In figure13b, the heat flows through the interface with the thermal barrier. In these results, the temperature at the lateral diameter of the NP stays below the melting point throughout the simulation because of the lesser energy being deposited in a-SiO_2 near this part of the interface. If the enhanced *e-ph* coupling is taken into account, the heating in the NP is increasing and even more efficient (see Figure 13c), since the energy is now deposited directly in the Au lattice. The heat accumulation is even stronger (see Figure 13d), when the insulance of the interface is also taken into account. To put the insulance reported in [42] in a perspective, it corresponds to μm thick layer of gold.

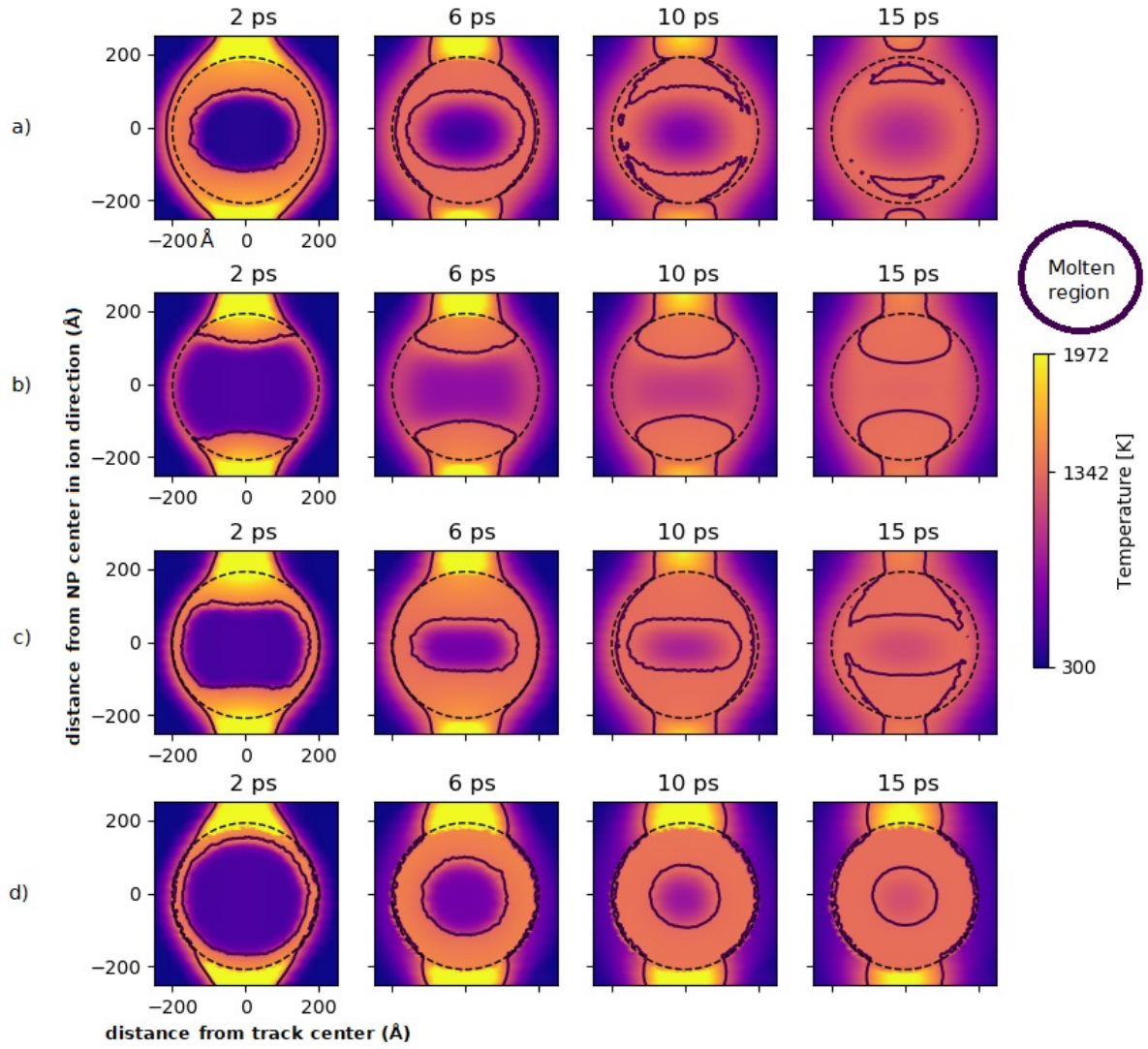

Figure 13: Temperature evolution of d = 40 nm spherical NPs with a) thermally transparent interface, b) 4.1 eV [38] barrier c) 4.1 eV barrier and interface scattering [41], and d) 4.1 eV barrier, electronic scattering and lattice insulance [42]. The NP is outlined by the dashed black line. The solid contour lines indicate the regions with atomic temperature above Au melting point.

6. Conclusion

The results of the present work show that the heat evolution in metal nanoparticles embedded in an insulating material is strongly dependent on the accuracy of the description of physical processes in the metal-insulator interface. The role of the interface was more substantial if the size of the nanoparticle was d$\geq$ 40 nm NPs. The heat dynamics in the nanoparticles with d $\leq$ 20 nm, the interface effects were much less significant. The common trend which we observed in all simulations employing different models of processes near the interface was that the melting of the nanoparticle started always at the interface. This observation is in line with the previous numerical results. However, our work shows that the driving mechanism for melting, and the related quantities of the total molten volume or heating and cooling rates, depend on several interface phenomena, that were not considered in previous works. The approaches for taking some of these phenomena into account developed here lay the basis for further theoretical work and comparisons with experiments.

Acknowledgments

We gratefully acknowledge the Academy of Finland NANOIS project for financial support and the IT Centre of Science CSC in Espoo, Finland and the Finnish Grid and Cloud Infrastructure (FGCI) for providing CPU resources.

Appendices

A. Implementation validity test

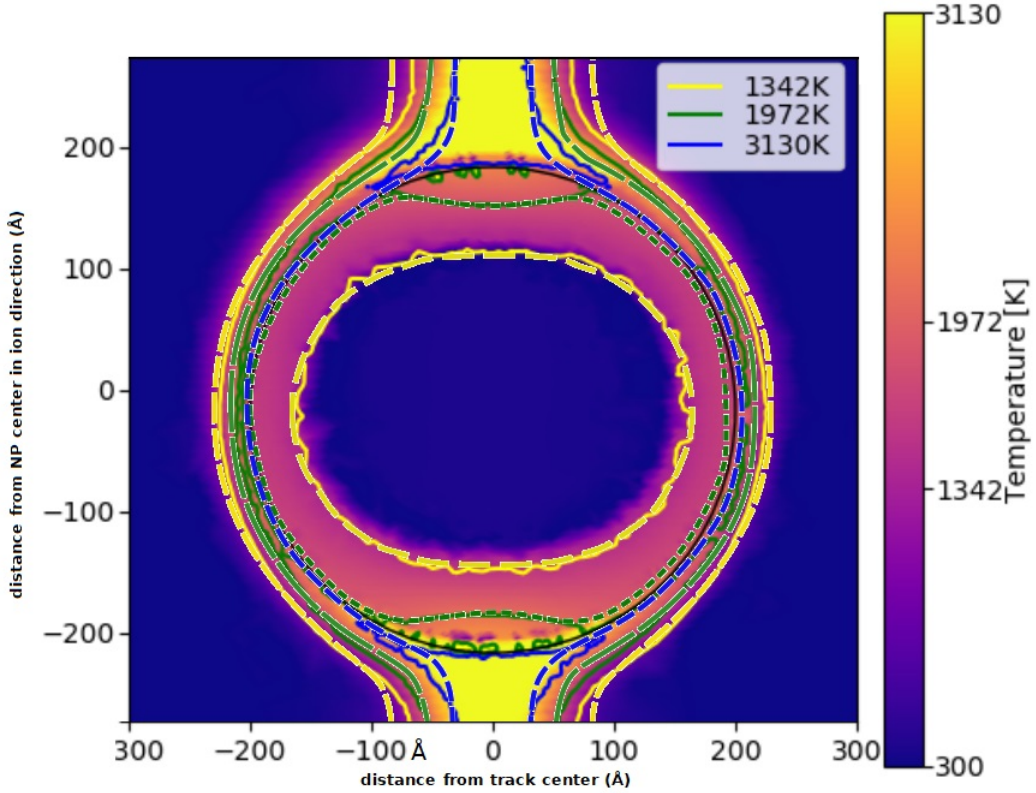

Figure 14: Validity test. Models produce similar results for d = 40 nm NP with with non-restricted heat flow through the NP-dielectric interface. Solid lines: this paper, dashed lines extracted from [33] as comparison.

B. FEM implementation of the two temperature model

We used a modified version of finite element code FEMOCS [34, 36] to run our TTM calculations. The modified version has two 3D heat solvers in FEMOCS but the Nottingham heating term described in [36] is replaced with a e-p coupling term (+ for atomic - for electronic) $G \cdot (T_e - T_a)$.

We used identical meshes for both the electronic and the lattice solvers so the corresponding temperatures could be imported for each point. Neumann boundary condition was added to the interface between lattice SiO_2 and Au solvers for both electronic and lattice heat conduction.

The total flux Q through an area A of the NP surface is

$$Q = \frac{T_{\mathrm{SiO_2}} - T_{\mathrm{Au}}}{R_{\mathrm{SiO_2}} + R_{\mathrm{Au}}} = \frac{T_{\mathrm{SiO_2}} - T_{\mathrm{Au}}}{\frac{\Delta x}{A\kappa_{\mathrm{SiO_2}}} + \frac{\Delta x}{A\kappa_{\mathrm{Au}}}} \tag{12}$$

This expression can be derived by considering heat conduction through thin slabs of thickness Δx at an interface of two heat conductivities, but here Δx is used as an adjustable parameter set to 1.0 Å. This parameter is chosen to be large enough for numerical stability, but sufficiently small not obstruct the heat flow artificially. The model gives an agreement with the results by Dufour et al. [33] (Appendix A). In 12, R_{Au} and $R_{\mathrm{SiO_2}}$ are the thermal resistances of the slabs. When writing this boundary condition in terms of flux density (q = Q/A, as in 4)

$$q = \frac{1}{\alpha}(T_{\mathrm{SiO_2}} - T_{\mathrm{Au}}) = \frac{T_{\mathrm{SiO_2}} - T_{\mathrm{Au}}}{\frac{\Delta x}{\kappa_{\mathrm{SiO_2}}} + \frac{\Delta x}{\kappa_{\mathrm{Au}}}} \tag{13}$$

the quantities depicted by the terms in the denominator are called thermal insulances. However, these are also sometimes confusingly called resistances, even though the units do match with the ISO standard [43]. The symbol for insulance is M.

α is described in Section 4. The boundary conditions was used for both electronic and lattice equations, i.e. the temperatures T and heat conductivities κ refer to electron and lattice values in the equations, respectively. By formulating the heat conduction through the Au/SiO_2 interface using a Neumann boundary condition, limiting the heat flux is simple. In the case of the interface between the electronic solvers, the flux is limited by $\frac{E_{high}(T)}{E_{total}(T)}$ so that

$$q = \frac{E_{high}(T)}{E_{total}(T)} \frac{T_{\mathrm{SiO_2}} - T_{\mathrm{Au}}}{\frac{\Delta x}{\kappa_{\mathrm{SiO_2}}} + \frac{\Delta x}{\kappa_{\mathrm{Au}}}}. \tag{14}$$

C. Two temperature model parameters

We used parameters same parameters for the two temperature model as in [33] for comparability.

	SiO_2	Au
g($Wcm^{-3}K^{-1}$)	$1.25 \cdot 10^{13}$	$2.3 \cdot 10^{10}$
ρ(g/cm^{-3})	2.32	19.3
T_m(K)	1972	1337
T_v(K)	3223	3130
Q_m(J/g)	142	63.7
Q_v(J/g)	4715	1645

Table 1: Material parameters for Au and silica. Melting and vaporization points T_m and T_v, and corresponding latent heats Q_m, and Q_v are added to atomic heat capacities around phase transition points. See [33] for details.

In table 1 e-p coupling constant g is an approximation from the value of quarz from [44] and is based on experimentally fitted mean energy-diffusion length. The value of g for gold is from [45] and is calculated from $g = \frac{\pi^4 (k_B n_e v)^2}{18 K_e(T_e)}$. Material densities are used to get correct electron densities and initial energy depositions from SRIM and to Waligorski distribution in [35].

Lattice thermal conductivity and specific heat were compiled in [33]. They cite [20], [46], [47], and [48]. For gold atomic heat conductivity relation $K_a = C_a v_s \alpha / 3$ was used where C_a and phonon mean free path α are from classical statistical physics and v_s the speed of sound in gold [33].

The melting temperature of silica was chosen by authors of [33] so that it is exactly in the middle of 1900 K $\pm$ 500 K which was the range given by many sources before.

For electronic parameters for gold were taken using the free electron gas model. Authors in [33] used formula $C_e(T_e) = (\pi^2 k_B n_e / 2)(T_e / T_F)$ for $T_e > \frac{3}{\pi^2} T_F$ and high temperature classical value $C_e = \frac{3}{2} k_B n_e$ above the value. Thermal conductivity for gold was taken using relation $K_e = C_e D_e$ using $D_e(T_e)$ from [49] as cited by [33] and approximating $D_e(T_e)$ to be $300 \frac{D(300K)}{T_e}$

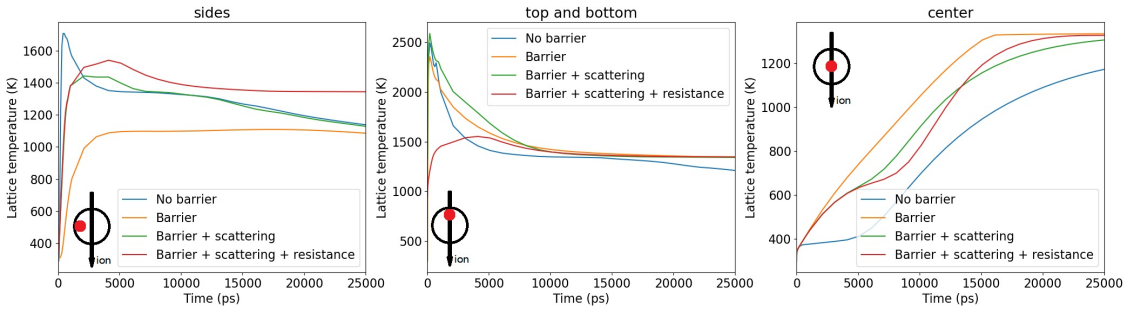

Figure 16: Lattice temperature as a function of time in sides, top and bottom, and in the center of the NP. From same simulations as Figure 13

below $T_{lim} = \frac{D(300K)}{D_{min}}$ and D_{min} above it, where $D(300K) = 150$ cm^{2}s^{-1} and $D_{min} = 2$ cm^{2}s^{-1}.

Dielectrics were approximated by free electron gas for hot electrons based on the work in [44]) with a linearly increasing value from 0 to 9 eV to approximate that below the bandgap energy, only part of the electrons is ionized. Specific heat of 1 Jcm^{-3}K and thermal conductivity of 2 Wcm^{-1}K^{-1} were used.

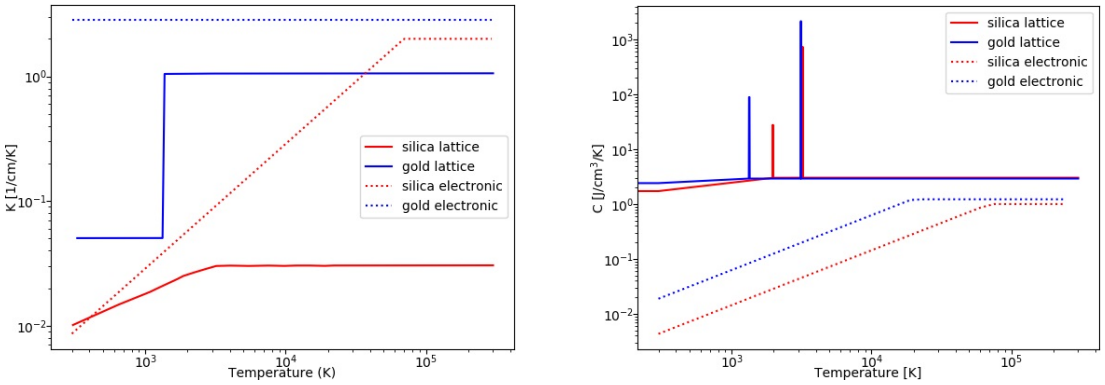

Figure 15: K and C values used in two temperature model calculations. See [33].

D. Time-temperature behaviour of different interface conditions

Figure 16 shows the comparison from Figure 13 in an alternative form. In Figure 16 it is easier to see that as long as there is no lattice resistance, the heating of the sides is fairly similar without the

barrier and with the barrier when surface scattering is included. This is because in both cases the heat is deposited very close to the NP interface and thermal conductivity in Au is much higher than in silica. What can also be observed is that, in the case with lattice resistance, the temperatures do not initially go as high as with the other three cases because the energy deposited in the silica side does not enter the NP. However, after a few picoseconds, these differences in temperature near the top and bottom vanish.

[1] Stefan A Maier, Pieter G Kik, Harry A Atwater, Sheffer Meltzer, Elad Harel, Bruce E Koel, and Ari AG Requicha. Local detection of electromagnetic energy transport below the diffraction limit in metal nanoparticle plasmon waveguides. *Nature Materials*, 2(4):229–232, 2003.

[2] Amanda J Haes, Shengli Zou, George C Schatz, and Richard P Van Duyne. A nanoscale optical biosensor: the long range distance dependence of the localized surface plasmon resonance of noble metal nanoparticles. *The Journal of Physical Chemistry B*, 108(1):109–116, 2004.

[3] Aleksi A Leino, Olli H Pakarinen, Flyura Djurabekova, and Kai Nordlund. A study on the elongation of embedded au nanoclusters in sio2 by swift heavy ion irradiation using md simulations. *Nuclear Instruments and Methods in Physics Research Section B: Beam Interactions with Materials and Atoms*, 282:76–80, 2012.

[4] Aleksi A Leino, OH Pakarinen, Flyura Djurabekova, Kai Nordlund, Patrick Kluth, and Mark C Ridgway. Swift heavy ion shape transformation of au nanocrystals mediated by molten material flow and recrystallization. *Materials Research Letters*, 2(1):37–42, 2014.

[5] EA Dawi, AM Vredenberg, G Rizza, and Marcel Toulemonde. Ion-induced elongation of gold nanoparticles in silica by irradiation with ag and cu swift heavy ions: track radius and energy loss threshold. *Nanotechnology*, 22(21):215607, 2011.

[6] Ovidio Peña-Rodríguez, Alejandro Prada, José Olivares, Alicia Oliver, Luis Rodríguez-Fernández, Héctor G Silva-Pereyra, Eduardo Bringa, José Manuel Perlado, and Antonio Rivera. Understanding the ion-induced elongation of silver nanoparticles embedded in silica. *Scientific reports*, 7(1):1–9, 2017.

[7] C D'orleans, JP Stoquert, C Estournes, JJ Grob, D Muller, JL Guille, Mireille Richard-Plouet, C Cerruti, and F Haas. Elongated co nanoparticles induced by swift heavy ion irradiations. *Nuclear Instruments and Methods in Physics Research Section B: Beam Interactions with Materials and Atoms*, 216:372–378, 2004.

[8] S Klaumünzer. Modification of nanostructures by high-energy ion beams. *Nuclear Instruments and Methods in Physics Research Section B: Beam Interactions with Materials and Atoms*, 244(1):1–7, 2006.

[9] Koichi Awazu, Xiaomin Wang, Makoto Fujimaki, Junji Tominaga, Hirohiko Aiba, Yoshimichi Ohki, and Tetsuro

Komatsubara. Elongation of gold nanoparticles in silica glass by irradiation with swift heavy ions. *Physical Review B*, 78(5):054102, 2008.

[10] Koichi Awazu, Xiaomin Wang, Tetsuro Komatsubara, Jun Watanabe, Yuki Matsumoto, Shin'ichi Warisawa, and Sunao Ishihara. The fabrication of aligned pairs of gold nanorods in sio2 films by ion irradiation. *Nanotechnology*, 20(32):325303, 2009.

[11] EA Dawi, G Rizza, MP Mink, AM Vredenberg, and FHPM Habraken. Ion beam shaping of au nanoparticles in silica: Particle size and concentration dependence. *Journal of Applied Physics*, 105(7):074305, 2009.

[12] P Kluth, R Giulian, DJ Sprouster, CS Schnohr, AP Byrne, DJ Cookson, and MC Ridgway. Energy dependent saturation width of swift heavy ion shaped embedded au nanoparticles. *Applied Physics Letters*, 94(11):113107, 2009.

[13] DK Avasthi, YK Mishra, Fouran Singh, and JP Stoquert. Ion tracks in silica for engineering the embedded nanoparticles. *Nuclear Instruments and Methods in Physics Research Section B: Beam Interactions with Materials and Atoms*, 268(19):3027–3034, 2010.

[14] Mark C Ridgway, Raquel Giulian, David J Sprouster, Patrick Kluth, Leandro Langie Araújo, DJ Llewellyn, AP Byrne, Felipe Kremer, Paulo Fernando Papaleo Fichtner, G Rizza, et al. Role of thermodynamics in the shape transformation of embedded metal nanoparticles induced by swift heavy-ion irradiation. *Physical Review Letters*, 106(9):095505, 2011.

[15] H Amekura, N Ishikawa, N Okubo, Mark C Ridgway, Raquel Giulian, K Mitsuishi, Y Nakayama, Ch Buchal, S Mantl, and N Kishimoto. Zn nanoparticles irradiated with swift heavy ions at low fluences: Optically-detected shape elongation induced by nonoverlapping ion tracks. *Physical Review B*, 83(20):205401, 2011.

[16] YK Mishra, F Singh, DK Avasthi, JC Pivin, D Malinovska, and E Pippel. Synthesis of elongated au nanoparticles in silica matrix by ion irradiation. *Applied Physics Letters*, 91(6):063103, 2007.

[17] Hiro Amekura, Patrick Kluth, Pablo Mota-Santiago, Isac Sahlberg, Ville Jantunen, Aleksi A Leino, Henrique Vázquez, Kai Nordlund, Flyura Djurabekova, N Okubo, et al. Vaporlike phase of amorphous si o 2 is not a prerequisite for the core/shell ion tracks or ion shaping. *Physical Review Materials*, 2(9):096001, 2018.

[18] James F. Ziegler and Jochen P. Biersack. *The Stopping and Range of Ions in Matter*, pages 93–129. Springer US, Boston, MA, 1985.

[19] G Rizza, PE Coulon, V Khomenkov, C Dufour, I Monnet, M Toulemonde, S Perruchas, T Gacoin, D Mailly, X Lafosse, et al. Rational description of the ion-beam shaping mechanism. *Physical Review B*, 86(3):035450, 2012.

[20] A Meftah, F Brisard, JM Costantini, E Dooryhee, M Hage-Ali, M Hervieu, JP Stoquert, F Studer, and

M Toulemonde. Track formation in sio 2 quartz and the thermal-spike mechanism. *Physical Review B*, 49(18):12457, 1994.

[21] IM Lifshits, MI Kaganov, and LV Tanatarov. On the theory of radiation-induced changes in metals. *Journal of Nuclear Energy. Part A. Reactor Science*, 12(1-2):69–78, 1960.

[22] SI Anisimov, BL Kapeliovich, TL Perelman, et al. Electron emission from metal surfaces exposed to ultrashort laser pulses. *Zh. Eksp. Teor. Fiz*, 66(2):375–377, 1974.

[23] AA Leino, SL Daraszewicz, Olli Heikki Pakarinen, K Nordlund, and F Djurabekova. Atomistic two-temperature modelling of ion track formation in silicon dioxide. *EPL (Europhysics Letters)*, 110(1):16004, 2015.

[24] Aleksi A Leino, OH Pakarinen, Flyura Djurabekova, Kai Nordlund, Patrick Kluth, and Mark C Ridgway. Swift heavy ion shape transformation of au nanocrystals mediated by molten material flow and recrystallization. *Materials Research Letters*, 2(1):37–42, 2014.

[25] Galvin S Khara, Samuel T Murphy, and Dorothy M Duffy. Dislocation loop formation by swift heavy ion irradiation of metals. *Journal of Physics: Condensed Matter*, 29(28):285303, 2017.

[26] H Dammak and A Dunlop. Tem observations of iron and nickel foils irradiated by mev fullerenes at room temperature. *Nuclear Instruments and Methods in Physics Research Section B: Beam Interactions with Materials and Atoms*, 146(1-4):285–289, 1998.

[27] Patrick Kluth, CS Schnohr, Olli H Pakarinen, Flyura Djurabekova, DJ Sprouster, Raquel Giulian, Mark C Ridgway, AP Byrne, Christina Trautmann, DJ Cookson, et al. Fine structure in swift heavy ion tracks in amorphous sio 2. *Physical review letters*, 101(17):175503, 2008.

[28] Henrique Vázquez and Flyura Djurabekova. Ultrafast phase transitions in polyamorphic materials triggered by swift heavy ion impacts. *Physical Review Materials*, 5(6):065603, 2021.

[29] M Sall, I Monnet, F Moisy, C Grygiel, S Jublot-Leclerc, S Della-Negra, M Toulemonde, and E Balanzat. Track formation in iii-n semiconductors irradiated by swift heavy ions and fullerene and re-evaluation of the inelastic thermal spike model. *Journal of Materials Science*, 50(15):5214–5227, 2015.

[30] O Osmani, N Medvedev, M Schleberger, and B Rethfeld. Energy dissipation in dielectrics after swift heavy-ion impact: a hybrid model. *Physical Review B*, 84(21):214105, 2011.

[31] Elisabeth Gruber, Pierre Salou, Lorenz Bergen, Mourad El Kharrazi, Elie Lattouf, Clara Grygiel, Yuyu Wang, Abdenacer Benyagoub, Delphine Levavasseur, Jimmy Rangama, et al. Swift heavy ion irradiation of caf2–from grooves to hillocks in a single ion track. *Journal of Physics: Condensed Matter*, 28(40):405001, 2016.

[32] A Kamarou, W Wesch, E Wendler, A Undisz, and M Rettenmayr. Swift heavy ion irradiation of inp: Thermal spike modeling of track formation. *Physical Review B*, 73(18):184107, 2006.

[33] Ch Dufour, V Khomenkov, G Rizza, and M Toulemonde. Ion-matter interaction: the three-dimensional version of the thermal spike model. application to nanoparticle irradiation with swift heavy ions. *Journal of Physics D: Applied Physics*, 45(6):065302, 2012.

[34] Mihkel Veske, Andreas Kyritsakis, Kristjan Eimre, Vahur Zadin, Alvo Aabloo, and Flyura Djurabekova. Dynamic coupling of a finite element solver to large-scale atomistic simulations. *Journal of Computational Physics*, 367:279–294, 2018.

[35] M.P.R. Waligórski, R.N. Hamm, and R. Katz. The radial distribution of dose around the path of a heavy ion in liquid water. *International Journal of Radiation Applications and Instrumentation. Part D. Nuclear Tracks and Radiation Measurements*, 11(6):309–319, 1986.

[36] Mihkel Veske, Andreas Kyritsakis, Flyura Djurabekova, Kyrre Ness Sjobak, Alvo Aabloo, and Vahur Zadin. Dynamic coupling between particle-in-cell and atomistic simulations. *Physical Review E*, 101(5):053307, 2020.

[37] Mermin David N. Ashcroft Neil W. *Solid state physics*. Holt, Rinehart and Winston, New York, London, 1976.

[38] VV Afanas' ev, Michel Houssa, Andre Stesmans, and MM Heyns. Band alignments in metal–oxide–silicon structures with atomic-layer deposited al 2 o 3 and zro 2. *Journal of applied physics*, 91(5):3079–3084, 2002.

[39] Yee-Chia Yeo, Tsu-Jae King, and Chenming Hu. Metal-dielectric band alignment and its implications for metal gate complementary metal-oxide-semiconductor technology. *Journal of applied physics*, 92(12):7266–7271, 2002.

[40] Pierre-Eugéne Coulon, Julia Amici, Marie-Claude Clochard, Vladimir Khomenkov, Christian Dufour, Isabelle Monnet, Clara Grygiel, Sandrine Perruchas, Christian Ulysse, Ludovic Largeau, et al. Ion-shaping of embedded gold hollow nanoshells into vertically aligned prolate morphologies. *Scientific reports*, 6(1):1–12, 2016.

[41] Patrick E Hopkins, Jared L Kassebaum, and Pamela M Norris. Effects of electron scattering at metal-nonmetal interfaces on electron-phonon equilibration in gold films. *Journal of Applied Physics*, 105(2):023710, 2009.

[42] Mihai G Burzo, Pavel L Komarov, and Peter E Raad. Thermal transport properties of gold-covered thin-film silicon dioxide. *IEEE Transactions on Components and Packaging Technologies*, 26(1):80–88, 2003.

[43] International Organization for Standardization (ISO 80000-5:2019). Quantities and units — part 5: Thermodynamics.

[44] M Toulemonde, JM Costantini, Ch Dufour, A Meftah, E Paumier, and F Studer. Track creation in sio2 and

bafe12o19 by swift heavy ions: a thermal spike description. *Nuclear Instruments and Methods in Physics Research Section B: Beam Interactions with Materials and Atoms*, 116(1-4):37–42, 1996.

[45] ZG Wang, Ch Dufour, E Paumier, and M Toulemonde. The se sensitivity of metals under swift-heavy-ion irradiation: a transient thermal process. *Journal of Physics: Condensed Matter*, 6(34):6733, 1994.

[46] David R Lide. *CRC handbook of chemistry and physics*. CRC press, 2006.

[47] Green D W Perry R H. *Perry's Chemical Engineers' Handbook*. New York: McGraw-Hill, 1984.

[48] YS Touloukian, RK Kirby, RE Taylor, and TYR Lee. Thermophysical properties of matter. *New York: IFI/Plenum*, page 89, 1970.

[49] Yu V Martynenko and Yu N Yavlinskii. Cooling of the electron gas of a metal at high temperatures. In *Soviet Physics Doklady*, volume 28, page 391, 1983.